Project No. 12-3923

Microscopic Fuel Particles Produced by Self-Assembly of Actinide Nanoclusters on Carbon Nanomaterials

Mission Supporting Transformative Research

Chongzheng Na
University of Notre Dame

Dan Vega, Federal POC
Jon Carmack, Technical POC

NEUP Nuclear Energy University Programs
U.S. Department of Energy

Microscopic Fuel Particles Produced by Self-Assembly of Actinide Nanoclusters

Project 12-3923

Final Report

Chongzheng Na and Peter C. Burns
University of Notre Dame

in Collaboration with

Bruce K. McNamara and Edgar C. Buck
Pacific Northwest National Laboratory

1. Abstract

Many consider further development of nuclear power to be essential for sustained development of society; however, the fuel forms currently used are expensive to recycle. In this project, we sought to create the knowledge and knowhow that are needed to produce nanocomposite materials by directly depositing uranium nanoclusters on networks of carbon-based nanomaterials. The objectives of the proposed work were to (1) determine the control of uranium nanocluster surface chemistry on nanocomposite formation, (2) determine the control of carbon nanomaterial surface chemistry on nanocomposite formation, and (3) develop protocols for synthesizing uranium-carbon nanomaterials. After examining a wide variety of synthetic methods, we show that synthesizing graphene-supported UO_2 nanocrystals in polar ethylene glycol compounds by polyol reduction under boiling reflux can enable the use of an inexpensive graphene precursor graphene oxide in the production of uranium-carbon nanocomposites in a one-pot process. We further show that triethylene glycol is the most suitable solvent for producing nanometer-sized UO_2 crystals compared to monoethylene glycol, diethylene glycol, and polyethylene glycol. Graphene-supported UO_2 nanocrystals synthesized with triethylene glycol show evidence of heteroepitaxy, which can be beneficial for facilitating heat transfer in nuclear fuel particles. Furthermore, we show that graphene-supported UO_2 nanocrystals synthesized by polyol reduction can be readily stored in alcohols, preventing oxidation from the prevalent oxygen in air. Together, these methods provide a facile approach for preparing and storing graphene-supported UO_2 nanocrystals for further investigation and development under ambient conditions.

2. Objectives, Efforts and Accomplishments

Many consider further development of nuclear power to be essential for the sustained development of our society using low-carbon baseload energy supplies.[1, 2] Currently, there are 71 reactors under construction in the world. Future nuclear reactors are expected to be more accident-tolerant, modularized for rapid assembly and mobility, and operated with fuels that are easy to disassemble for reprocessing (i.e., removal of radioactive fission products and extraction of fissile materials). To provide designers of future reactors with fuel options superior to conventional bulk uranium dioxide (UO_2), research has begun to focus on UO_2 nanocrystals for potential benefits that include a lowered sintering temperature[3] thanks to melting-point suppression and the increased kinetics of UO_2 dissolution in reprocessing[4] thanks to the increase of specific surface area. In addition, using UO_2 nanocrystals presents a new opportunity for blending UO_2 with highly conductive nanomaterials to provide novel solutions for the long-standing issue regarding uranium dioxide's low thermal conductivity. Recent simulations have shown that blending UO_2 with 10% of graphene by volume can increase the thermal conductivity of fuel particles by more than 30%, which can not only increase the rate of energy extraction but also improve reactor safety by lowering the fuel operating temperature.[5]

The overall objective of the project was to create a foundation of knowledge in support of a new type of reactor fuel that could capture the accident-tolerant advantages of carbon-actinide composites mentioned above, but in a form that could be readily recycled and that is relatively

inexpensive to manufacture. Towards achieving this goal, we have utilized the nano-scale control of actinides and carbon chemistry. We have investigated the use of a self-supporting grid of carbon nanomaterials onto which networks of actinide nanoclusters were deposited. Specific research objectives included (1) determine the control of uranium nanocluster surface chemistry on nanocomposite formation, (2) determine the control of carbon nanomaterial surface chemistry on nanocomposite formation, and (3) develop protocols for synthesizing uranium-carbon nanomaterials. In the following sections, we will provide detailed descriptions of research efforts and research for each of the specific objectives. We will show that after a wide variety of synthetic methods were tested, polyol reduction has emerged as a facile approach for depositing well-defined single crystal uranium dioxide (UO_2) nanocrystals on graphene sheets, which is promising for improving thermal conductivity because UO_2 nanocrystals are intimately bonded to graphene through heteroepitaxy. Heteroepitaxy is known to induce coupling effects between metal oxide and graphene.[6] In graphene-UO_2 nanocomposite, strong phonon-phonon coupling between UO_2 nanocrystal and graphene can lead to an improved long-range thermal conduction, in which graphene serves as the thermal-conduction channel thereby bypassing the highly resisting UO_2 grain boundaries.

(1) Control of Uranium Nanocluster Surface Chemistry

We have synthesized uranium-carbon nanocomposites using both complex uranium cage clusters and simple uranyl nitrate as precursors. As shown below, using the same carbon support (i.e., graphene oxide), uranium can be deposited in the forms of uranium cage clusters, two-dimensional uranium sheets, or uranium dioxide nanocrystals.

U_{60} cage cluster on graphene oxide. Uranium peroxide cage clusters (e.g., U_{60} in Figure 1a) are a class of newly discovered actinide supermolecules. They can be readily created by bridging uranyl ions with peroxo bridges under oxidative conditions and in the presence of counter cations (e.g., Li^+ colored in purple in Figure 1a). The formation of cage clusters is proposed as a novel technique for recovering uranium from spent fuel; therefore, it is interesting to investigate the possibility of create uranium-carbon nanocomposites using cage clusters. We have created U_{60}-graphene oxide (GO) nanocomposite by directly mixing the two constituents together. The U_{60} nanoclusters were prepared by oxidizing uranyl (prepared form nitrate salt) by peroxide in aqueous solution. The nanoclusters crystalized in aqueous solution in approximately one week. The crystal was taken out of the original solution, rinsed, and re-dissolved in water. Graphene oxide was prepared by chemically exfoliating high-quality naturally occurring graphite by a mixture of sodium nitrate, potassium permanganate, and sulfuric acid at 98^{o}C in ice bath (a.k.a. the modified Hummer's method). Graphene oxide was extracted from the reactive solution by acetone and cleaned with DI water. The two materials were then mixed together in deionized water at diluted concentrations.

In the nanocomposite shown in Figure 1b, U_{60} clusters (dark spots) are homogeneously distributed between graphene oxide sheets. The clusters, which have an average diameter 2.2(±0.5) nm (Figure 1c), are well isolated from each other under electrostatic repulsion originating from their negative charges. High-resolution transmission electron micrograph

reveals the lattice fringes of graphene oxide sheets that are laid on top of U_{60} clusters (Figure 1d).

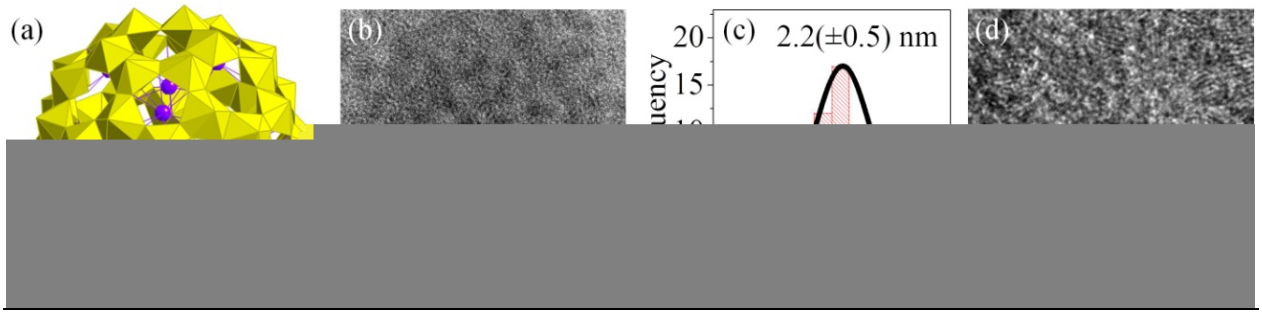

Figure 1. (a) Schematic diagram of the U_{60} cluster; (b) Transmission electron microscope (TEM) image of the homogeneously distributed U_{60} cluster; (c) Size distribution of the dark spots in b; (d) High-resolution TEM image of one typical dark spot.

Studtite on graphene oxide. By increasing the concentrations of graphene oxide to approximately 1 g L^{-1}, we can create an acidic solution with a pH as low as 3 – 4. It is known that U_{60} nanoclusters are not stable under acidic conditions. The inherent acidity of graphene oxide can then destabilize the curved peroxide bond in U_{60} and stretched the curved structure into a sheet of studtite. As shown in Figure 2, studtite ($[(UO_2)O_2(H_2O)_2]\bullet 2H_2O$, a) and graphene oxide ($C_8H_3O_4$ with intercalated water and cations, Figure 2b) are both two-dimensional layered nanomaterials. The sandwich nanocomposite is created by laying alternating layers of studtite and graphene oxide on top of each other (Figure 2c). X-ray diffraction of the nanocomposite shows distinctive patterns of studtite and graphene oxide (Figure 2d). The diffraction angles for the layered constituents are determined by fitting the diffraction patterns with Lorentzian functions, which permits the estimation of lattice spacings according to Bragg's law. The lattice spacings are estimated to be 5.93(±0.01) Å and 8.45/9.54(±0.04) Å (higher value for K-intercalated layers, cf. Figure 2b) for studtite and graphene oxide, which are consistent with literature values. The numbers of studtite and graphene oxide layers in the alternating sandwich configuration are determined to be 31(±2) and 12(±2) using Scherrer's equation (cf. Figure 2c). Scanning electron microscopy (SEM, Figure 2e) and energy-dispersive X-ray spectroscopy mapping (Figure 2f) show homogeneous mixing of uranium and carbon. The resulting nanocomposite can be readily casted into macroscopic forms (Figure 2g).

UO_2 on graphene oxide. Monodispersed GO is very easy to be produced and shows good dispersion due to the abundant functional group (-COOH, O<, and -OH) on the surface. As a result, GO exhibits negative charge which can easy to interact with cations. Uranyl is the main structure of uranium, which suggests that we can produce uranium-GO nanocomposites by mixing GO and uranyl directly. Figure 3a shows the schematic diagram of the formation mechanism of *in-situ* synthesis of uranium oxide-GO nanocomposite. Due to the charge interaction between uranyl and GO, uranyl is easily coated on the surface of GO. Bound uranyl may be reduced by the functional groups on GO to nucleate and form uranium oxide nanoparticles. Energy-dispersive X-ray spectroscopy (EDS) (Figure 3b) shows the appearance of uranium element on GO. The monodispersion of uranium oxide nanoparticles can be observed

through the low magnified TEM images (Figure 3c and d). The high-resolution TEM image (Figure 3e) reflects the typical lattice fringes of the UO_x nanoparticles. The sizes of the nanoparticles are about 2 nm.

Figure 2. Studtite-carbon nanocomposite prepared from U_{60} cage cluster and graphene oxide.

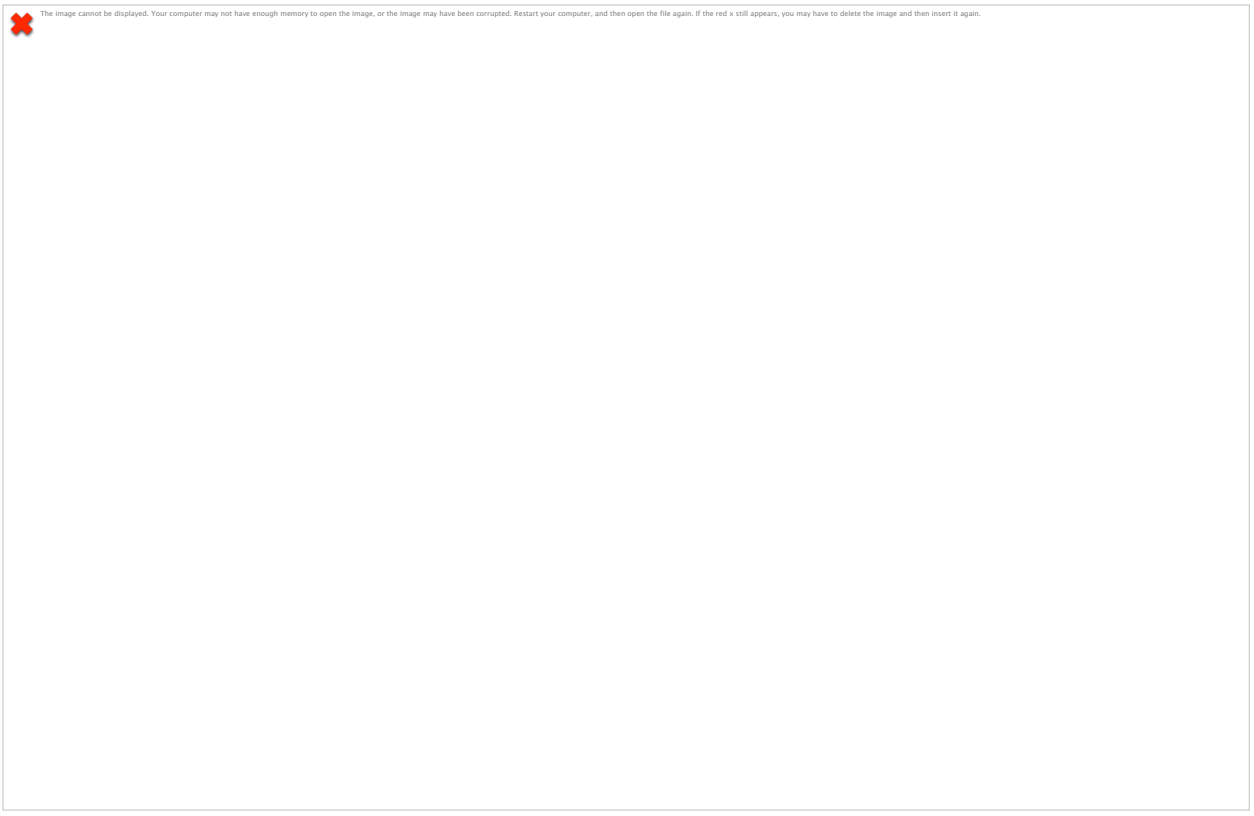

Figure 3. (a) Schematic diagram of the formation mechanism of uranium oxide-GO nanocomposite; (b) Energy-dispersive X-ray spectroscopy of the nanocomposite; (c, d, and e) from low to high magnified and high resolution TEM images of the nanocomposite.

(2) Control of Carbon Nanomaterial Surface Chemistry

The deposition of uranium nanophases is not limited to the use of graphene oxide as support. Below, we show that uranium nanoclusters and uranium dioxide nanocrystals can also be deposited on reduced graphene oxide and inside carbon nanotubes, respectively.

U_{60} cage cluster on reduced graphene oxide. Monolayer dispersion of U_{60} clusters on reduced graphene oxide (rGO) by organic amine linker. U_{60} cluster is produced by bridging uranyl ions with peroxo bridges under oxidative conditions and showing negative charge, which can be stable in the presence of counter cations (Figure 4a). rGO is two-dimensional layered nanomaterials with lower negative charge than graphene oxide, which is suitable for the positive charged surface functionalization. A new type of U_{60}-rGO nanocomposite was synthesized through the charge interaction between organic amine linker and U_{60} clusters. The rGO was first treated with a molecule (3-phenylpropan-1-amine) which contains both the positive charged amine group and phenyl group. After the functionalizaiton, rGO is easy to connect with U60 cluster via the charge interaction (Figure 4a). TEM image shows that small dark domains are homo-distributed on the rGO sheet reflecting that the monolayer dispersion

of U_{60} clusters (Figure 4b). High-resolution TEM image (Figure 4c) shows the lattice fringes of the nanoparticles. Combining with the selected-area electron diffraction (SAED, which is not presented here), the nanoparticles are assigned to UO_2. This method is ready to be generally applied to bind negative charged nanoparticles or clusters on rGO surface.

Figure 4. (a) Schematic diagram of the U_{60}-rGO nanocomposite formation mechanism; (b and c) show the low-magnification and high-resolution TEM images of the U_{60}-rGO nanocomposite.

U-filled carbon nanotubes. Mono-dispersed uranium oxide nanoparticles filled into multi-walled carbon nanotubes (MWCNTs). MWCNTs have been used to fill different metal/metal oxide owing to the large cavity. Previously, the most popular driven-force for the CNT filling is capillary force, which usually shows low filling intensity. Here, we produce the uranium-carbon nanocomposite by filling MWCNTs with mono-dispersed uranium oxide nanoparticles through a liquid phase filling technique. Hydrophobic uranium oxide nanoparticles have been synthesized by high-temperature thermal decomposition of uranyl oleate. So we filled the carbon nanotube with uranyl oleate first. Due to the hydrophobic property of the oleate, the filling efficiency of uranyl is high, which guarantees the final filling density of uranium oxide nanoparticles. TEM images reflect that uranium oxide nanoparticles with the mono-distribution (about 5 nm in diameter) are appeared in the channel of CNTs (Figure 5a and b). Different loading intensities can be observed in the TEM image (Figure 5c). This may be due to the different length of the CNTs or the concentration of uranyl oleate. By controlling the concentration, loading time, loading temperature, and loading pressure of uranium precursor, uranium filled CNT nanocomposite can be synthesized with different loading intensity.

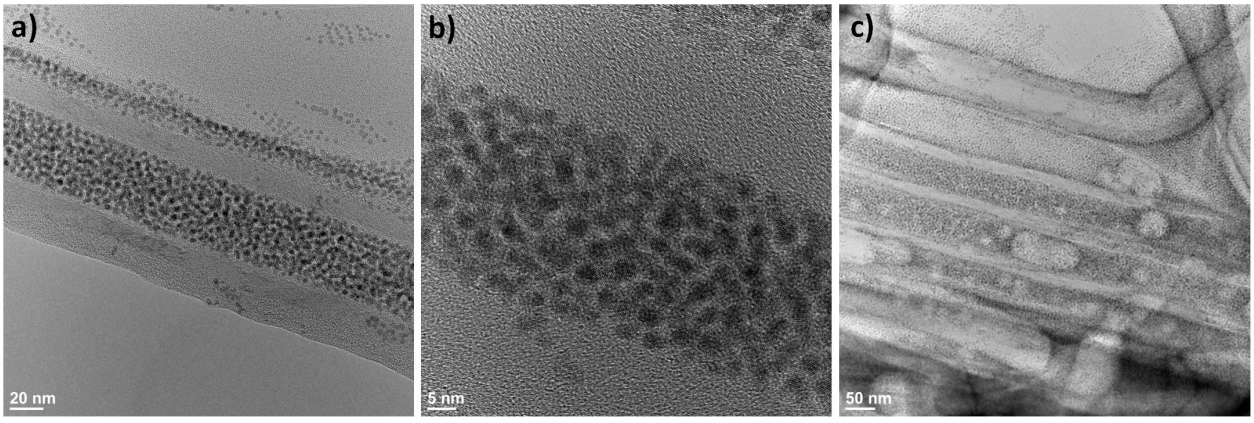

Figure 5. (a) TEM image of a typical segment of carbon nanotube filled with mono-dispersed uranium oxide nanoparticles; (b) The magnified TEM image of a; (c) TEM image of carbon naotubes with different filling density of uranium oxide nanoparticles.

(3) Optimal Protocol for Synthesizing Uranium-Carbon Nanomaterials

Per the survey results presented in section (1) and (2), we believe that the deposition of uranium dioxide nanocrystals on graphene represents the most promising route to creating well-defined and well-control U-C nanocomposites. In this section, we present the logic and formulation of our synthetic method for optimizing the deposition of uranium dioxide nanocrystals on graphene sheets using polyol reduction.

A well-established route for synthesizing graphene-supported metal and metal oxide nanocrystals uses graphene oxide as a graphene precursor.[7-9] Graphene oxide can be prepared as single-layer carbon sheets from natural graphite by chemical exfoliation that breaks apart π-π stacking.[10-13] Because of the use of strong acids and oxidants in chemical exfoliation, graphene oxide contains a rich number of hydroxyl, carboxyl, and epoxyl surface groups, making it hydrophilic and dispersible in polar solutions.[14, 15] The majority of the oxygen-containing functional groups can be removed upon reduction, which converts carboxylate, hydroxyl, and epoxyl groups back to sp^2 carbon, creating graphene sheets (formally known as reduced graphene oxide to be distinguished from graphene prepared from bottom-up synthesis).[16, 17] The reduction of graphene oxide can be incorporated into the synthesis of nanocrystals in a one-pot process when polar solvents are used to accommodate the dispersion of graphene oxide, producing graphene-supported nanocrystals.[8, 18, 19]

Previously, UO_2 nanocrystals having a nominal diameter of 10 nm or less have been made by employing ferrous,[20] amine-assisted,[21-23] radiolytic,[3] electrochemical,[24] and microbial mediated reduction of U(VI) salts.[25-27] Among the existing methods, the thermal reduction of uranyl acetylacetonate ($UO_2(C_5H_7O_2)_2$) by oleylamine is a scalable chemical method carried out in nonpolar solvents such as octadecene, which offers good control of nanocrystal structure, size, and morphology.[21, 23] Because UO_2 nanocrystals, like most oxide nanoparticles, are hydrophilic, synthesis in nonpolar solvents requires the use of capping agents such as oleic acid to give the nanocrystals a hydrophobic surface in order to stabilize them against aggregation in nonpolar

solvents. In principle, it is possible to switch nanocrystal surface wettability from being hydrophobic to being hydrophilic through ligand exchange so that they can be dispersed in polar solvents;[28] however, successful experimental protocols are not yet available for UO_2 nanocrystals. Obviously, using graphene oxide as the precursor for preparing graphene-supported UO_2 requires a synthetic route performed in polar solvents.

A widely used synthetic method for preparing metal oxide nanocrystals, such as those made of iron oxide and copper oxide, is polyol reduction in ethylene glycols (EGs; $(CH_2)_{2n}O_{n-1}(OH)_2$, n = 1, 2, 3, 4 …).[29-31] EG compounds are mild reductants that can be oxidized to aldehydes, then carboxylic acids, and eventually carbon dioxide and protons.[32-34] They have sufficient reducing potential to transform graphene oxide to graphene;[7-9] however, whether the polyol reduction method can be used to prepare graphene-supported UO_2 nanocrystals has not been investigated. One of the two objectives of this study is, therefore, to determine the possibility of and conditions for preparing graphene-supported UO_2 nanocrystals by polyol reduction in a one-pot operation. The second objective of this study is to determine how to handle the resulting graphene-supported UO_2 nanocrystals under ambient conditions so that they can be stored and studied without oxidizing U(IV) back to U(VI).
We begin our investigation of synthesizing graphene-supported UO_2 by selecting an ethylene glycol compound with an appropriate chain length in the absence of graphene oxide. Unsupported UO_2 nanocrystals are synthesized by the reduction of uranyl acetylacetone in the EG solution heated to boiling reflux. As outlined in Figure 6, the synthesis protocol includes two main steps. First, uranyl (UO_2^{2+}) nitrate aqueous solution is mixed with acetylacetone to produce $UO_2(acac)_2$, which is collected by precipitation.[35, 36] Second, $UO_2(acac)_2$ is dissolved in an ethylene glycol solvent in a one-pot operation. The reactive solution is heated to boiling reflux under argon protection. The boiling point of the EG solvent increases with the chain length.[37]

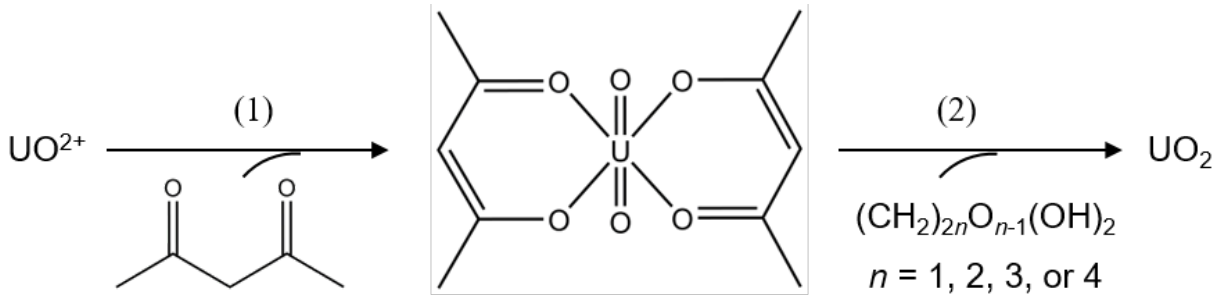

Figure 6. Polyol reduction process investigated for the synthesis of uranium dioxide nanocrystals.

Figure 7 shows the synthetic products prepared with the four EG solvents. As the aliphatic chain of ethylene glycol increases in length, the color of the product solution changes from orange to yellow, black, and then grey (Figure 7a – d). The yellow-to-black color transition is a well-known characteristic associated with the U(VI)-to-U(IV) reduction. The observation of the gradual color change with the increasing EG chain length indicates that the reduction of U(VI) is incomplete

with MEG and DEG but complete with TEG and PEG. Close examination using transmission electron microscopy shows that nanowires are formed with MEG (Figure 7e) while nanoparticles are formed with DEG, TEG, and PEG (Figure 7f – h). Further analysis using powder X-ray diffraction indicates that the nanowires produced by MEG are ianthinite ($U(UO_3)_5O_7 \cdot 10H_2O$),[38] a U(VI) oxide hydrate (Figure 7i). For the sample synthesized with DEG, the characteristic diffraction maxima for UO_2 become prominent, confirming the formation of UO_2 nanocrystals. However, the presence of equally prominent reflections from ianthinite (e.g., 004 at 12^o) indicates the existence of a significant amount of ianthinite as an impurity. The reflections for ianthinite become indiscernible for the TEG product, suggesting that the amount of U(VI) impurity has become negligible (Figure 7j). The XRD patterns for the nanocrystals match well with those for bulk UO_2 (i.e., uraninite),[39] although the peaks are broadened in the synthetic sample due to diminished particle size (as expected). Compared to the product of TEG, the sample obtained from PEG shows broad reflections with barely discernible peaks, suggesting that the sample lacks long-range ordering and thus is amorphous in nature. The formation of amorphous materials is an indication that the reducing power of PEG is too potent, which creates a high level of supersaturation favouring instantaneous nucleation without much crystal growth.[19]

Figure 7. Reduction of uranyl acetylacetone by (a, e, i) ethylene glycol, (b, f, j) diethylene glycol, (c, g, k) triethylene glycol, (d, h, l) polyethylene glycol. (a – d) Digital graphs. (e – h) Transmission electron micrographs. Scale bars: *e*, 1 μm; *f* – *g*, 5 nm. (i – l) Powder X-ray diffraction. Vertical

lines mark reflections from ianthinite (JCPDS 12-272; dash lines) and uraninite (JCPDS 65-285; solid lines).

Under TEM, nanocrystals made with TEG are identifiable as particles around 3 nm in diameter (Figure 7g). The lattice fringes of the nanocrystals, although visible, are not sharp, which suggests the presence of a relatively high percentage of defects. The defect concentration can be greatly reduced by adding PVP and preheating TEG to reflux temperature, which provides an improved temperature control. As shown in Figure 8a, nanocrystals synthesized with preheated TEG have sharp lattice fringes. Nanocrystals shown in Figure 7g and 8a are slightly aggregated when they are deposited on the TEM grid. The aggregation of nanoparticles often occurs during sample preparation because the evaporation of solvent creates capillary force that pulls nanocrystals together. Evaporation-induced aggregation can be prevented by replacing PVP with either citrate or ascorbate, which provides improved steric repulsion that can resist capillary pulling.[40] Citric acid is thermally stable at the synthesis temperature,[41] while ascorbic acid likely decomposes into products containing carboxylate formed by opening the lactone ring.[42] As shown in Figure 8b and c, citrate and ascorbate-capped nanocrystals exhibit a more uniform and isolated distribution on TEM grids, which offers the opportunity for accurately measuring the sizes of the nanocrystals. According to measurements made with 228 isolated nanocrystals, their nominal diameter is d_{TEM} = 2.8(±0.3) nm by fitting the histogram with a Gaussian function, as shown in Figure 3d. This value agrees well with the value estimated from XRD peak broadening. According to Scherrer's Equation, $d = 0.89\,\lambda\,\beta^{-1}\cos^{-1}\theta$ where Cu Kα X-ray wavelength λ = 1.54 Å.[43] For the {111} peak with diffraction angle ϑ = 14.00(±0.03) deg and broadening at half the maximum intensity β = 0.050(±0.004) radian, d_{XRD} = 2.85(±0.23) nm. According to these estimates, the coefficient of variation is computed at 8 – 10%, suggesting the nanocrystal population has a near mono-dispersed size distribution.[44-46]

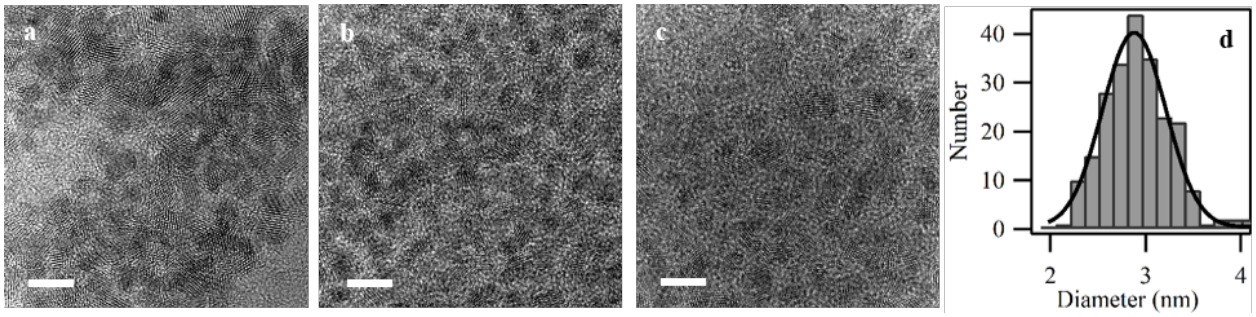

Figure 8. Uranium dioxide nanocrystals synthesized with (a) pre-heated triethylene glycol as well as (b) citrate or (c) ascorbate capping. (d) Statistical analysis of nominal diameter of nanocrystals in *b* and *c*. Scale bar: 5 nm.

To synthesize graphene-supported UO_2, single-layer graphene oxide is added to TEG with uranyl acetylacetone. Under boiling reflux, TEG reduces both uranyl acetylacetone and graphene oxide. As shown in Figure 9a, nano-sized UO_2 deposits are formed uniformly on graphene sheets, suggesting a switch of crystallization mechanism from homogenous to heterogeneous nucleation. As expected, reduction removes a significant amount of oxygen functional groups

on graphene oxide (61% → 34%; Figure S1) without changing the overall sheet thickness (i.e., 1.7 nm; Figure S2).[47] XRD confirms that the deposits are UO_2, as shown in Figure 9b. Compared to the XRD patterns shown in Figure 7k, UO_2 deposited on graphene shows an intensified (002) reflection. The lack of a distinctive peak at $2\theta = 26.6^{o}$ corresponding to the 002 reflection of graphite[48] confirms that graphene sheets are made of single layers of carbon without a significant amount of multi-layer sheets consisting of π-π stacking. The lack of peaks around $2\theta = 11^{o}$ suggests that there is also no stacking of graphene oxide sheets through water intercalation. As shown in Figure 9c, high resolution TEM reveals that UO_2 on graphene has a shape of parallelogram. Statistical analysis estimates that the parallelograms have a nominal diameter of 2.49(±0.46) nm, as illustrated in Figure 9d.

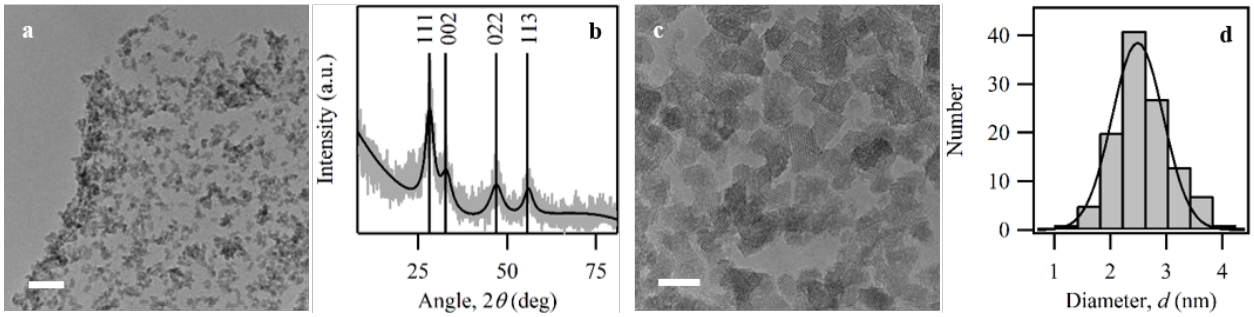

Figure 9. Uranium dioxide nanocrystals decorated on graphene sheets. (a) Transmission electron micrograph (TEM). (b) Powder X-ray diffraction. (c) High resolution TEM. (d) Statistical analysis of nanocrystal size. Scale bars: *a*, 20 nm; *c*, 5 nm.

Further analyses of the lattice structures of unsupported and graphene-supported UO_2 suggest that heteroepitaxy is likely the mechanism responsible for UO_2 growth on graphene. An unsupported UO_2 nanocrystal synthesized in TEG is visualized using high resolution TEM (HRTEM) in Figure 10a. The HRTEM image shows that the nanocrystal has a face-centred close (FCC) packing structure and is seated with the (110) plane facing upward and almost perfectly perpendicular to the electron beam. The orientation of the nanocrystal is determined by comparing the Fast Fourier transform (FFT) of the HRTEM image, as presented in Figure 10b, with the electron diffraction pattern of a UO_2 standard.[39] Using CrystalMaker®, we have identified the prominent electron diffraction spots of the nanocrystal, several of which are marked in Figure 10c.

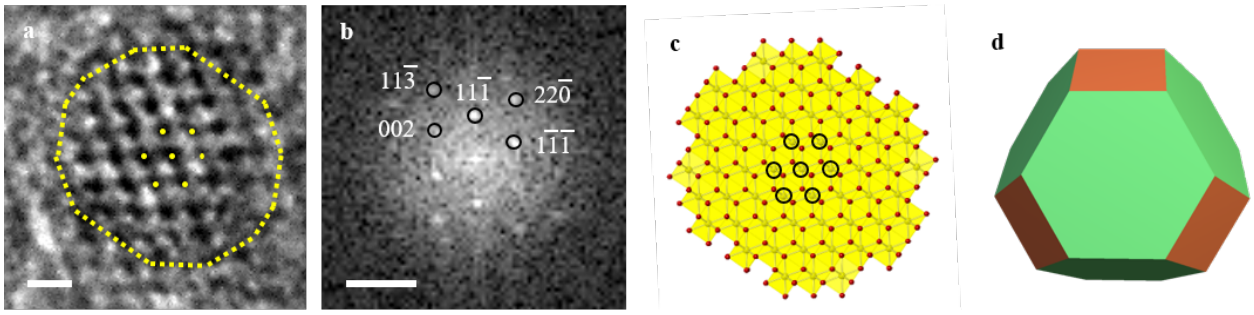

Figure 10. Structure and morphology of suspended UO_2 nanocrystals. (a) High resolution transmission electron micrograph of a single UO_2 nanocrystal. To compare with the molecular model in *c*, the near surface uranium atoms are connected by yellow dash lines and the distinctive pattern of uranium atoms in the (110) planes are marked with seven yellow dots. (b) Fast Fourier transform of *b*, showing electron diffraction spots. (c) A model molecule of truncated UO_2 nanocrystal $U_{281}O_{792}$ viewed from the [110] direction. Seven black circles are used to illustrate the pattern marked by the seven yellow dots in *a*. (d) A model of truncated octahedron. Atoms in color: U, yellow; O, red. Scale bars: *a*, 5 Å; *b*, 5 nm^{-1}.

The individual nanocrystal in Figure 10a is further analyzed with the assistance of a molecular model. As shown in Figure 10c, the molecule, which is terminated with oxygen atoms on the surface, has the shape of a truncated octahedron. The molecule consists of 281 uranium atoms and 792 oxygen atoms and has a mass $m = 132 \times 10^{-21}$ g. According to the uraninite density $\rho = 1.01 \times 10^{7}$ g m^{-3},[39] the model molecule has a volume of 1.3×10^{-26} m^3 and a nominal diameter of 2.8 nm. To aid comparison, we have marked the distinctive patterns of seven uranium atoms in the centre of the (110) plane on both the HRTEM image and the molecular model in Figure 10a and c, which match perfectly. We have also marked the edge of the model molecule in the HRTEM image with dashed lines in Figure 10a. These results suggest that UO_2 nanocrystals suspended in alcohols are likely in the shape of a truncated octahedron, as illustrated in Figure 10d. Several uranium atoms of the nanocrystal are located outside the model boundary, suggesting that the nanocrystal surface can be rugged on the atomic level.

A close examination of UO_2 nanocrystals deposited on graphene, as shown in Figure 11a, indicates a preferred orientation and thus possible heteroepitaxy. FFT performed on representative crystals show that the nanocrystals still have the FCC structure but that they are always seated with the [110] zone axis perpendicular to the underlying graphene sheet. As shown in Figure 11b – d, the diffraction spots of individual crystals are formed by the reflections of {111} and {002} planes. Three types of rotational transformations are found among the nanocrystals, consistent with the 3-fold symmetry of graphene, as demonstrated in the HRTEM of Figure 11e, which shows UO_2 nanocrystals as hexagons with clear lattice fringes. An alternative explanation of the orientation is due to the formation of a network of UO_2 nanocrystals, which connect with one another through specific planes. However, such an explanation is inconsistent with the presence of isolated islands of UO_2 crystals on graphene (cf. Figure 9a and b).

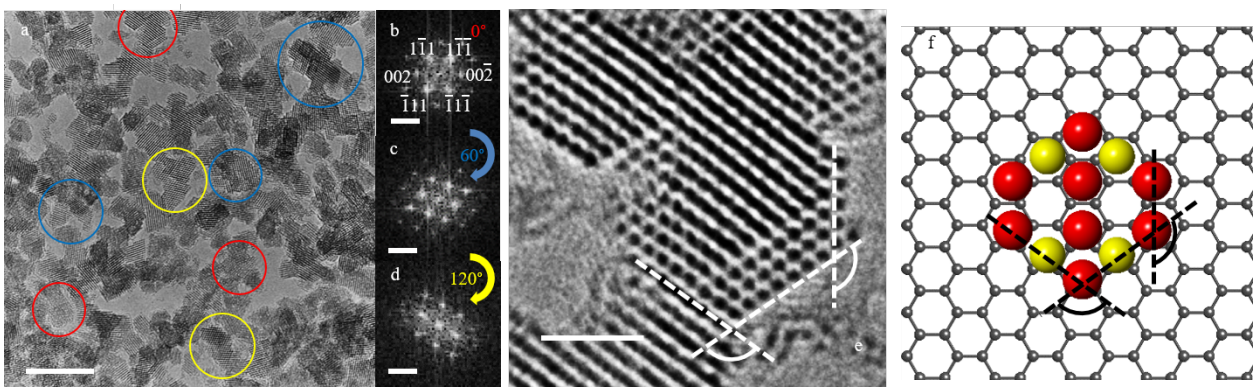

Figure 11. Heteroepitaxy of UO_2 nanocrystals deposited on graphene. (a) Transmission electron micrograph (TEM) showing nanocrystals with equivalent orientations. (b, c, d) Fast Fourier transform of nanocrystals in *a* with 0^o, 60^o, and 120^o rotations, respectively. (e) High resolution TEM showing the sharp edges of nanocrystals. (f) Molecular model showing heteroepitaxy. Atoms in color: U, yellow; O, red. Scale bars: *a*, 10 nm; *b* – *d*, 5 nm^{-1}; *e*, 2 nm.

The epitaxial interface between graphene and UO_2 is further modelled in Figure 11f, with U and O atoms on top of the center of the six-member carbon rings. The distance between U and O is 2.37 Å and that between O and O is 2.73 Å. The angles of the hexagonal UO_2 are 109° and 125°, which are identical with the angles shown in the model. Because the distance between two adjacent six-member carbon rings is 2.46 Å and the angles for the six-member carbon rings beneath the hexagonal UO_2 are 120°, the structures of UO_2 and graphene have mismatch on the atomic level, which may have constrained the size of the nanocrystals. Epitaxial linkages with similar degrees of mismatch have been observed at the interfaces of graphene with ruthenium,[49] copper,[50] molybdenum sulfide (MoS_2),[51] bismuth selenide (Bi_2Se_3),[52] and gold cyanide (AuCN).[53] Density functional theory calculations suggest that the interfaces are likely formed by graphene donating π electrons to the overgrowing phases.[53] A distinctive feature of the weak van der Waals bond, compared to the much stronger covalent[54] and ionic[55] bonds, is the preferred formation of islands and nanowires instead of continuous films.[56] This is consistent with the UO_2 islands over graphene observed in our experiments, as shown in Figure 11a.

In theory, the hypothesized heteroepitaxial growth mechanism can be validated by comparing the lattice of UO_2 and that of the underlying graphene. To achieve the atomic resolution of a single-layer graphene or graphene oxide, the observation requires a transmission electron aberration-corrected microscope operated under a low beam energy.[57] Although a beam of electrons accelerated at tens to hundreds of kilovolts can provide atomic resolutions in TEM, the actual resolution is restricted by spherical and chromatic aberrations.[58] In addition, single-layer graphene is fragile and can be readily damage by electrons having an energy above 85 keV.[59, 60]

3. List of Publications

Results obtained from this project have been mainly disseminated through the publication of the following peer-reviewed journal articles:

1. Ma, H.; Wang, H.; Burns, P. C.; McNamara, B. K.; Buck, E. C.; Na, C. Synthesis and preservation of graphene-supported uranium dioxide nanocrystals. *Journal of Nuclear Materials*. **2016**, 475, 113-122.
2. Ma, H.; Wang, H.; Wu, T.; Na, C. Highly active layered double hydroxide- derived cobalt nano-catalysts for p-nitrophenol reduction. *Applied Catalysis B: Environmental*. **2016**, 180, 471-479.
3. Duster, T. A.; Na, C.; Bolster, D.; Fein, J. B. Transport of single-layered graphene oxide nanosheets through quartz and iron oxide-coated sand columns. *Journal of Environmental Engineering*. **2016**, 04016079.
4. Krylova, G.; Na, C. Photoinduced crystallization and activation of amorphous titanium dioxide. *Journal of Physical Chemistry C*. **2015**, 119, 12400-12407.
5. Krylova, G.; Yashan, H.; Hauck, J. G.; Burns, P. C.; McGinn, P. J.; Na, C. Microwave-assisted solution-liquid-solid synthesis of single-crystal copper indium sulfide nanowires. *Crystal Growth & Design*. **2015**, 15, 2859-2866.
6. Wang, H.; Na, C. Chemical bath deposition of aluminum oxide buffer on curved surfaces for growing aligned carbon nanotube arrays. *Langmuir*. **2015**, 31, 7401-7409.
7. Ma, H.; Na, C. Isokinetic temperature and size-controlled activation of ruthenium-catalyzed ammonia borane hydrolysis. *ACS Catalysis*. **2015**, 5, 1726-1735.
8. Wu, T.; Wang, H.; Liu, F.; Burns, P. C.; Na, C. Multi-body coalescence in Pickering emulsions. *Nature Communications*. **2015**, doi: 10.1038/ncomms6929.
9. Ma, H.; Wang, H.; Na, C. Microwave-assisted optimization of platinum-nickel nanoalloys for catalytic water treatment. *Applied Catalysis B: Environmental*. **2015**, 163, 198-204.
10. Duster, T. C.; Szymanowski, J. E. S.; Na, C.; Showalter, A. R.; Bunker, B. A.; Fein, J. B. Surface complexation modeling of proton and metal sorption onto graphene oxide. *Colloids and Surfaces A: Physicochemical and Engineering Aspects*. **2015**, 466, 28-39.
11. Wang, H.; Na, C. Binder-free carbon nanotube electrode for electrochemical removal of chromium. *ACS Applied Materials & Interfaces*. **2014**, 6, 20309-20316.
12. Wang, H.; Ma, H.; Zheng, W.; An, D.; Na, C. Multifunctional and recollectable carbon nanotube ponytails for water purification. *ACS Applied Materials & Interfaces*. **2014**, 6, 9426-9434.
13. Wang, H.; Na, C. Synthesis of millimeter-long vertically aligned carbon nanotube arrays on aluminum oxide buffer prepared by layer-by-layer assembly of boehmite nanoplates. *Carbon*. **2014**, 66, 727-729.
14. Wang, H.; Dong, Z.; Na, C. Hierarchical carbon nanotube membrane supported gold nanoparticles for rapid catalytic reduction of p-nitrophenol. *ACS Sustainable Chemistry & Engineering*. **2013**, 1, 746-752. Featured in Front.
15. Wang, H.; Lin, K.; Jing, B.; Krylova, G.; Sigmon, G. E.; McGinn, P. J.; Zhu, Y.; Na, C. Removal of oil droplets from contaminated water using magnetic carbon nanotubes. *Water Research*. **2013**, 47, 4198-4205.

ERGY
ar Energy

Microscopic Fuel Particles Produced by Self-Assembly of Actinide Nanoclusters on Carbon Nanomaterials

OVERVIEW

s of future reactors with fuel options better than conventional
s, we seek to create uranium-carbon nanocomposites by
nanophases on self-supporting three-dimensional carbon
integration of uranium fuel with carbon moderator at the
provide unprecedented flexibility in controlling the size, powder
and recycling of fuel particles.

ontrol of uranium nanocluster surface chemistry on
formation
ontrol of carbon nanomaterial surface chemistry on
formation
ols for synthesizing uranium-carbon nanocomposites

IMPACT

Logical Path

Control of uranium nanocrystal chemistry
Control of carbon nanomaterial chemistry
→ Control of nanocomposite synthesis

Outcomes

1. Several types of microscopic nanocomposites produced by successfully assembling uranium nanoclusters on carbon nanomaterials
2. Improved understanding of uranium self-assembly in solution systems that are relevant to nuclear fuel fabrication
3. Postdoctoral fellows and graduate students who will be trained in nano-scale nuclear chemistry for America's energy future.

DETAILS

or: Chongzheng Na

ty of Notre Dame

r C. Burns (University of Notre Dame) and Bruce McNamara and
Northwest National Laboratory)

Total Funding Level: $440,000

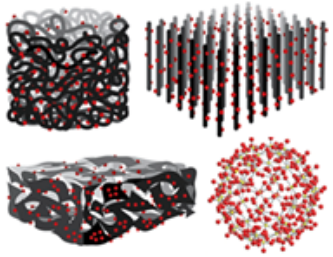

Daniel Vega

age #:
7-01

RESULTS

1. Synthesis and preservation of graphene-supported uranium dioxide nanocrystals. (*Journal of Nuclear Materials*, **2016**, 475, 113-122).
2. Highly active layered double hydroside-derived cobalt nano-catalysts for p-nitrophenol reduction (*Applied Catalysis B: Environmental*, **2016**, 180, 471 – 479).
3. Chemical bath deposition of aluminum oxide buffer on curved surfaces for growing aligned carbon nanotube arrays (*Langmuir*, **2015**, 31, 7401 – 7409).
4. Photoinduced crystallization and activation of amorphous titanium oxide (*Journal of Physical Chemistry C*, **2015**, 119, 12400 – 12407).
5. Microwave-assisted solution-liquid-solid synthesis of single-crystal indium sulfide nanowires (*Crystal Growth & Design*, **2015**, 15, 2859 – 2866).
6. Transition of nanoparticle reactivity between enthalpy- and entropy-controlled temperature regimes (*ACS Catalysis*, **2015**, 5, 1726 – 1735).
7. Multi-body coalescence in Pickering emulsions (*Nature Communications*, **2015**, doi:10.1038/ncomms6929).
8. Microwave-assisted reduction methods for synthesizing nanoparticles (*Applied Catalysis B: Environmental*, **2015**, 163, 198-204; Featured by *Nanowerk*).
9. Particle-graphene oxide interactions (*Journal of Environmental Engineering*, **2016**, 04016079; *Colloids and Surfaces A: Physicochemical and Engineering Aspects*, **2015**, 466, 28-39).
10. Electrochemical deposition of metal oxides on carbon nanotubes (*ACS Applied Materials & Interfaces*, **2014**, 6, 20309-20316).
11. Carbon nanotube ponytails as nanoparticle support (*ACS Applied Materials & Interfaces*; **2014**, 6, 9426-9434; Featured by *Nanowerk*).
12. Millimeter-long vertically aligned CNT forests (*Carbon*, **2014**, 66, 727-729.).
13. Vertically aligned carbon nanotube forests as nanoparticle support (*ACS Sustainable Chemistry & Engineering*, **2013**, 1, 746-752; Featured in cover).
14. Carbon nanotubes as particle support (*Water Research*, **2013**, 47, 4198-4205).

References Cited

1. United States Department of Energy, *Nuclear Energy Research and Development Roadmap*2010.
2. M. Nicholson, T. Biegler, and B.W. Brook, "How carbon pricing changes the relative competitiveness of low-carbon baseload generating technologies," Energy, 36(1), 305-313 (2011).
3. T.M. Nenoff, B.W. Jacobs, D.B. Robinson, P.P. Provencio, J.Y. Huang, S. Ferreira, and D.J. Hanson, "Synthesis and low temperature in situ sintering of uranium oxide nanoparticles," Chemistry of Materials, 23(23), 5185-5190 (2011).
4. Y. Suzuki, S.D. Kelly, K.M. Kemner, and J.F. Banfield, "Nanometre-size products of uranium bioreduction," Nature, 419(6903), 134-134 (2002).
5. S.W. Lee, H.T. Kim, and I.C. Bang, "Performance evaluation of UO_2/graphene composite fuel and SiC cladding during LBLOCA using MARS-KS," Nuclear Engineering and Design, 257(0), 139-145 (2013).
6. E.H. Hwang, R. Sensarma, and S. Das Sarma, "Plasmon-phonon coupling in graphene," Physical Review B, 82(19), 195406 (2010).
7. H.-G. Jung, Y.S. Jeong, J.-B. Park, Y.-K. Sun, B. Scrosati, and Y.J. Lee, "Ruthenium-based electrocatalysts supported on reduced graphene oxide for lithium-air batteries," ACS Nano, 7(4), 3532-3539 (2013).
8. J.W. Lee, T. Ahn, D. Soundararajan, J.M. Ko, and J.-D. Kim, "Non-aqueous approach to the preparation of reduced graphene oxide/α-$Ni(OH)_2$ hybrid composites and their high capacitance behavior," Chemical Communications, 47(22), 6305-6307 (2011).
9. S.W. Oh, Z.-D. Huang, B. Zhang, Y. Yu, Y.-B. He, and J.-K. Kim, "Low temperature synthesis of graphene-wrapped $LiFePO_4$ nanorod cathodes by the polyol method," Journal of Materials Chemistry, 22(33), 17215-17221 (2012).
10. C. Schafhaeutl, "On the combination of carbon with silicon and iron, and other metals, forming the different species of cast iron, steel, and malleable iron," Phil. Mag., 16(570-590 (1840).
11. D. Li, M.B. Müller, S. Gilje, R.B. Kaner, and G.G. Wallace, "Processable aqueous dispersions of graphene nanosheets," Nature Nanotechnology, 3(101-5 (2008).
12. W.S. Hummers and R.E. Offeman, "Preparation of graphitic oxide," Journal of the American Chemical Society, 80(1339 (1958).
13. B.C. Brodie, "Sur le poids atomique du graphite," Ann. Chim. Phys., 59(466 (1860).
14. A. Lerf, H. He, M. Forster, and J. Klinowski, "Structure of graphite oxide revisited," Journal of Physical Chemistry B, 102(4477-4482 (1998).
15. W. Gao, L.B. Alemany, L. Ci, and P.M. Ajayan, "New insights into the structure and reduction of graphite oxide," Nature Chemistry, 1(403-8 (2009).
16. R. Fu, Z. Li, Y. Liang, F. Li, F. Xu, and D. Wu, "Hierarchical porous carbons: design, preparation, and performance in energy storage," New Carbon Materials, 26(3), 171-179 (2011).
17. Y. Xu, K. Sheng, C. Li, and G. Shi, "Self-assembled graphene hydrogel via a one-step hydrothermal process," ACS Nano, 4(7), 4324-4330 (2010).

18. Y. Liu, Y. Zhang, G. Ma, Z. Wang, K. Liu, and H. Liu, "Ethylene glycol reduced graphene oxide/polypyrrole composite for supercapacitor," Electrochimica Acta, 88(519-525 (2013).
19. H. Ma, H. Wang, and C. Na, "Microwave-assisted optimization of platinum-nickel nanoalloys for catalytic water treatment," Applied Catalysis B: Environmental, 163(0), 198-204 (2015).
20. E.J. O'Loughlin, S.D. Kelly, R.E. Cook, R. Csencsits, and K.M. Kemner, "Reduction of Uranium(VI) by Mixed Iron(II)/Iron(III) Hydroxide (Green Rust): Formation of UO2 Nanoparticles," Environmental Science & Technology, 37(4), 721-727 (2003).
21. H. Wu, Y. Yang, and Y.C. Cao, "Synthesis of colloidal uranium−dioxide nanocrystals," Journal of the American Chemical Society, 128(51), 16522-16523 (2006).
22. D. Hudry, C. Apostolidis, O. Walter, T. Gouder, E. Courtois, C. Kubel, and D. Meyer, "Controlled synthesis of thorium and uranium oxide nanocrystals," Chemistry - A European Journal, 19(17), 5297-5305 (2013).
23. N. Pinna, G. Garnweitner, M. Antonietti, and M. Niederberger, "A general nonaqueous route to binary metal oxide nanocrystals involving a C-C bond cleavage," Journal of the American Chemical Society, 127(15), 5608-5612 (2005).
24. D. Gil, R. Malmbeck, J. Spino, T. Fanghanel, and R. Dinnebier, "Nanoscale UO_2 and novel complex U(IV)-sulphate phase formation from electrolytically reduced uranyl sulphate solutions," Radiochimica Acta, 98(2), 77-89 (2010).
25. D.M. Singer, F. Farges, and G.E. Brown, "Biogenic nanoparticulate UO_2: Synthesis, characterization, and factors affecting surface reactivity," Geochimica Et Cosmochimica Acta, 73(12), 3593-3611 (2009).
26. S.Y. Lee, M.H. Baik, and J.W. Choi, "Biogenic formation and growth of uraninite (UO_2)," Environmental Science & Technology, 44(22), 8409-8414 (2010).
27. E.J. O'Loughlin, S.D. Kelly, R.E. Cook, R. Csencsits, and K.M. Kemner, "Reduction of uranium(VI) by mixed iron(II)/iron(III) hydroxide (green rust): Formation of UO_2 nanoparticies," Environmental Science & Technology, 37(4), 721-727 (2003).
28. R. Hong, N.O. Fischer, T. Emrick, and V.M. Rotello, "Surface PEGylation and ligand exchange chemistry of FePt nanoparticles for biological applications," Chemistry of Materials, 17(18), 4617-4621 (2005).
29. W. Cai and J. Wan, "Facile synthesis of superparamagnetic magnetite nanoparticles in liquid polyols," Journal of Colloid and Interface Science, 305(2), 366-370 (2007).
30. S.-W. Cao, Y.-J. Zhu, and J. Chang, "Fe_3O_4 polyhedral nanoparticles with a high magnetization synthesized in mixed solvent ethylene glycol-water system," New Journal of Chemistry, 32(9), 1526-1530 (2008).
31. M.H. Kim, B. Lim, E.P. Lee, and Y. Xia, "Polyol synthesis of Cu_2O nanoparticles: use of chloride to promote the formation of a cubic morphology," Journal of Materials Chemistry, 18(34), 4069-4073 (2008).
32. C. Bock, C. Paquet, M. Couillard, G.A. Botton, and B.R. MacDougall, "Size-Selected Synthesis of PtRu Nano-Catalysts: Reaction and Size Control Mechanism," Journal of the American Chemical Society, 126(25), 8028-8037 (2004).

33. L.-J. Chen, C.-C. Wan, and Y.-Y. Wang, "Chemical preparation of Pd nanoparticles in room temperature ethylene glycol system and its application to electroless copper deposition," Journal of Colloid and Interface Science, 297(1), 143-150 (2006).
34. F. Fievet, J.P. Lagier, B. Blin, B. Beaudoin, and M. Figlarz, "Homogeneous and heterogeneous nucleations in the polyol process for the preparation of micron and submicron size metal particles," Solid State Ionics, 32(3), 198-205 (1989).
35. A.M. Bhandari, S. Dubey, and R.N. Kapoor, "Uranyl soaps," Journal of the American Oil Chemists Society, 47(4), 115-116 (1970).
36. A.E. Comyns, B.M. Gatehouse, and E. Wait, "The chemistry of uranyl acetylacetone complex," Journal of the Chemical Society, 4655-4665 (1958).
37. D.R. Lide, *CRC Handbook of Chemistry and Physics*2006, New York: CRC Press.
38. P.C. Burns, R.J. Finch, F.C. Hawthorne, M.L. Miller, and R.C. Ewing, "The crystal structure of ianthinite, $[U_2^{4+}(UO_2)_4O_6(OH)_4(H_2O)_4](H_2O)_5$: a possible phase for Pu^{4+} incorporation during the oxidation of spent nuclear fuel," Journal of Nuclear Materials, 249(2–3), 199-206 (1997).
39. R.W.G. Wyckoff, *Crystal Structures*. 2nd ed1963, New York, New York: Interscience Publishers.
40. Q. Zhang, N. Li, J. Goebl, Z.D. Lu, and Y.D. Yin, "A systematic study of the synthesis of silver nanoplates: Is citrate a "magic" reagent?," Journal of the American Chemical Society, 133(46), 18931-18939 (2011).
41. M.I. Lorı´a-Bastarrachea, W. Herrera-Kao, J.V. Cauich-Rodrı´guez, J.M. Cervantes-Uc, H. Va´zquez-Torres, and A. Avila-Ortega, "A TG/FTIR study on the thermal degradation of poly(vinyl pyrrolidone)," J. Therm. Anal. Calorim., 104(737-742 (2011).
42. M. Rueda, A. Aldaz, and F. Sanchezburgos, "Oxidation of L-ascorbic acid and a gold electrode," Electrochimica Acta, 23(5), 419-424 (1978).
43. A.L. Patterson, "The Scherrer formula for X-ray particle size determination," Physical Review, 56(10), 978-982 (1939).
44. C.B. Murray, C.R. Kagan, and M.G. Bawendi, "Synthesis and characterization of monodisperse nanocrystals and close-packed nanocrystal assemblies," Annual Review of Materials Science, 30(545-610 (2000).
45. J. Xu, S. Li, J. Tan, Y. Wang, and G. Luo, "Controllable preparation of monodisperse O/W and W/O emulsions in the same microfluidic device," Langmuir, 22(19), 7943-7946 (2006).
46. H. Yuyama, T. Watanabe, G.-H. Ma, M. Nagai, and S. Omi, "Preparation and analysis of uniform emulsion droplets using SPG membrane emulsification technique," Colloids and Surfaces A: Physicochemical and Engineering Aspects, 168(2), 159-174 (2000).
47. O.C. Compton and S.T. Nguyen, "Graphene oxide, highly reduced graphene oxide, and graphene: Versatile building blocks for carbon-based materials," small, 6(6), 711-723 (2010).
48. P. Trucano and R. Chen, "Structure of graphite by neutron diffraction," Nature, 258(5531), 136-137 (1975).
49. P.W. Sutter, J.-I. Flege, and E.A. Sutter, "Epitaxial graphene on ruthenium," Nature Materials, 7(5), 406-411 (2008).

50. L. Gao, J.R. Guest, and N.P. Guisinger, "Epitaxial graphene on Cu(111)," Nano Letters, 10(9), 3512-3516 (2010).
51. Y. Shi, W. Zhou, A.-Y. Lu, W. Fang, Y.-H. Lee, A.L. Hsu, S.M. Kim, K.K. Kim, H.Y. Yang, L.-J. Li, J.-C. Idrobo, and J. Kong, "van der Waals epitaxy of MoS_2 layers using graphene as growth templates," Nano Letters, 12(6), 2784-2791 (2012).
52. W. Dang, H. Peng, H. Li, P. Wang, and Z. Liu, "Epitaxial heterostructures of ultrathin topological insulator nanoplate and graphene," Nano Letters, 10(8), 2870-2876 (2010).
53. W.C. Lee, K. Kim, J. Park, J. Koo, H.Y. Jeong, H. Lee, D.A. Weitz, A. Zettl, and S. Takeuchi, "Graphene-templated directional growth of an inorganic nanowire," Nature Nanotechnology, 10(5), 423-428 (2015).
54. H. Ma, H. Wang, T. Wu, and C. Na, "Highly active layered double hydroxide-derived cobalt nano-catalysts for *p*-nitrophenol reduction," Applied Catalysis B: Environmental, 180(471-479 (2016).
55. M.H. Yang and C.P. Flynn, "Growth of alkali halides by molecular-beam epitaxy," Physical Review B, 41(12), 8500-8508 (1990).
56. A.K. Geim and I.V. Grigorieva, "Van der Waals heterostructures," Nature, 499(7459), 419-425 (2013).
57. C. Gómez-Navarro, J.C. Meyer, R.S. Sundaram, A. Chuvilin, S. Kurasch, M. Burghard, K. Kern, and U. Kaiser, "Atomic Structure of Reduced Graphene Oxide," Nano Letters, 10(4), 1144-1148 (2010).
58. Ç.Ö. Girit, J.C. Meyer, R. Erni, M.D. Rossell, C. Kisielowski, L. Yang, C.-H. Park, M.F. Crommie, M.L. Cohen, S.G. Louie, and A. Zettl, "Graphene at the Edge: Stability and Dynamics," Science, 323(5922), 1705-1708 (2009).
59. R.S. Pantelic, J.C. Meyer, U. Kaiser, and H. Stahlberg, "The application of graphene as a sample support in transmission electron microscopy," Solid State Communications, 152(15), 1375-1382 (2012).
60. R.F. Egerton, "Choice of operating voltage for a transmission electron microscope," Ultramicroscopy, 145(85-93 (2014).